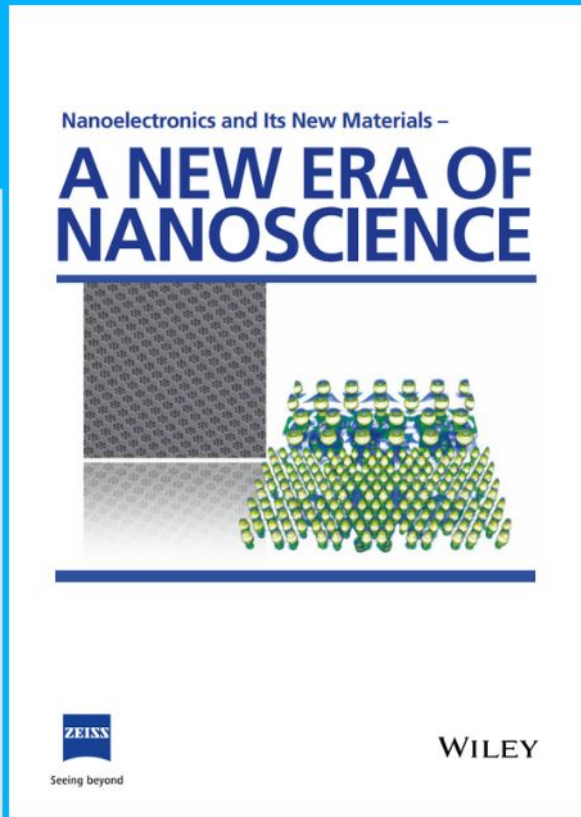




Nanoelectronics and Its New Materials – A NEW ERA OF NANOSCIENCE



Discover the recent advances in electronics research and fundamental nanoscience.

Nanotechnology has become the driving force behind breakthroughs in engineering, materials science, physics, chemistry, and biological sciences. In this compendium, we delve into a wide range of novel applications that highlight recent advances in electronics research and fundamental nanoscience. From surface analysis and defect detection to tailored optical functionality and transparent nanowire electrodes, this eBook covers key topics that will revolutionize the future of electronics.

To get your hands on this valuable resource and unleash the power of nanotechnology, simply download the eBook now. Stay ahead of the curve and embrace the future of electronics with nanoscience as your guide.



Seeing beyond

WILEY

Flexoelectric Domain Walls Originated from Structural Phase Transition in Epitaxial BiVO₄ Films

Pao-Wen Shao, Heng-Jui Liu, Yuanwei Sun, Mei Wu, Ren-Ci Peng, Meng Wang, Fei Xue, Xiaoxing Cheng, Lei Su, Peng Gao, Pu Yu, Long-Qing Chen, Xiaoqing Pan, Yachin Ivry, Yi-Chun Chen, and Ying-Hao Chu*

Polar domain walls in centrosymmetric ferroelastics induce inhomogeneity that is the origin of advantageous multifunctionality. In particular, polar domain walls promote charge-carrier separation and hence are promising for energy conversion applications that overcome the hurdles of the rate-limiting step in the traditional photoelectrochemical water splitting processes. Yet, while macroscopic studies investigate the materials at the device scale, the origin of this phenomenon in general and the emergence of polar domain walls during the structural phase transition in particular has remained elusive, encumbering the development of this attractive system. Here, it is demonstrated that twin domain walls arise in centrosymmetric BiVO₄ films and they exhibit localized piezoelectricity. It is also shown that during the structural phase transition from the tetragonal to monoclinic, the symmetry reduction is accompanied by an emergence of strain gradient, giving rise to flexoelectric effect and the polar domain walls. These results not only expose the emergence of polar domain walls at centrosymmetric systems by means of direct observation, but they also expand the realm of potential application of ferroelastics, especially in photoelectrochemistry and local piezoelectricity.

1. Introduction

Over the last decades, the conversion of green solar energy to electricity is an appealing strategy to minimize the enormous use of fossil fuels. Among oxide semiconductors, monoclinic scheelite bismuth vanadate BiVO₄ (BVO) is well known for its extraordinary photoelectrochemical effect. It also serves as an attractive candidate for photoanode, mainly because its adequate bandgap (2.4–2.6 eV)^[1,2] for effective absorption of visible light as well as due to its non-toxicity and high stability.^[3,4] Another interesting characteristic of BVO is ferroelasticity, which is one of the ferroic properties that displays the hysteresis behavior between stress and strain components. With a specific stress applied, the strain state is artificially manipulated accordingly, setting up a reversible switching mechanism similar to electrical switching of ferroelectrics.^[5]

P.-W. Shao, Y.-H. Chu
Department of Materials Science and Engineering
National Yang Ming Chiao Tung University
Hsinchu 30010, Taiwan
E-mail: yhchu@mx.nthu.edu.tw

H.-J. Liu
Department of Materials Science and Engineering
National Chung Hsing University
Taichung 40227, Taiwan

Y. Sun, M. Wu, P. Gao
International Center for Quantum Materials
School of Physics
Peking University
Beijing, China

Y. Sun, M. Wu, P. Gao
Electron Microscopy Laboratory
School of Physics
Peking University
Beijing, China

R.-C. Peng
School of Advanced Materials and Nanotechnology
Xidian University
Xi'an 710126, China

M. Wang, P. Yu
Department of Physics
Tsinghua University
Beijing, China


F. Xue, X. Cheng, L.-Q. Chen
Department of Materials Science and Engineering
The Pennsylvania State University
University Park, PA 16802, USA

L. Su, X. Pan
Department of Materials Science and Engineering
University of California
Irvine, CA 92697, USA

X. Pan
Department of Physics and Astronomy
University of California at Irvine
Irvine, CA 92697, USA

X. Pan
Irvine Materials Research Institute
University of California at Irvine
Irvine, CA 92697, USA

Y. Ivry
Department of Materials Science and Engineering Technion
Israel Institute of Technology
Haifa 3200003, Israel

 The ORCID identification number(s) for the author(s) of this article can be found under <https://doi.org/10.1002/sml.202107540>.

DOI: 10.1002/sml.202107540

Due to the coexistence of energy-degenerated structures of ferroelastics, domain boundaries give rise to inhomogeneity in these materials so that the local symmetry and properties differ from the bulk material.^[6] For example, ferroelectric domain walls initially can display higher photoconductivity mainly because the photo-generated carriers are separated by a strong electric field, accumulating at domain wall region due to the symmetry breaking.^[7,8] For centrosymmetric ferroelastics such as CaTiO₃, LaAlO₃, and BVO, estimated by Landau phenomenological theory,^[9] symmetry analysis,^[10] and second harmonic generation,^[11] the inversion symmetry breaks at ferroelastic domain wall.

In the previous study, BVO was reported showing polar ferroelastic domain walls within centrosymmetric lattice matrix.^[12] In this case, estimated by Landau free energy and considering Lifshitz invariant,^[13] incommensurate domain walls (i.e., W' wall) play the dominant role since the remaining internal stress from the second-order phase transition (i.e., tetragonal to monoclinic) is responsible for the orientation of W' walls,^[14] which is incompatible with specific crystal axis. Therefore, the emergence of BVO polar ferroelastic domain walls could be realized by the phase transition because the primary order parameter during transition is B_g symmetry, developed by the residual strain in ab plane.^[15,16] Different temperature dependent techniques including Raman spectroscopy,^[17] neutron diffraction,^[18] and X-ray diffraction (XRD)^[15] have been developed to determine that the transition from paraelastic phase (scheelite tetragonal) to ferroelastic one (monoclinic scheelite) occurs at 255 °C.^[2] However, the direct relationship between residual strain and polar domain walls in sub-micron scale remains challenging since the residual strain would be relaxed by defect formation, e.g., dislocation, grain boundary, etc. In this work, we fabricated epitaxial BVO films on Yttria-stabilized Zirconia (YSZ) single crystal substrate by pulsed laser deposition. The crystal structure and phase transition were studied in situ by a combination of XRD and transmission electron microscopy (TEM). It turns out that flexoelectric domain walls originate from phase transition process, and the corresponding domain structures of BVO film were probed by piezoresponse force microscopy (PFM). Our results provide new insights on the roles of strain gradient at domain walls of ferroelastics and induced flexoelectricity in corresponding domain configuration.

2. Results and Discussion

BVO exhibits ferroelasticity at room temperature with the centrosymmetric space group of I_2/b .^[14,19] Experimentally, twin domain structures can be managed in epitaxial BVO film

(monoclinic I_2/b , $a = 5.204$ Å, $b = 5.101$ Å, $c = 11.69$ Å, $\gamma = 89.6^\circ$) deposited on YSZ substrate (cubic, $a = 5.153$ Å). **Figure 1a** reveals a typical out-of-plane XRD theta-2theta scan of the BVO/YSZ heterostructure. A superior crystallinity is conformed due to only the presence of YSZ(00L) and BVO(00L) diffraction peaks together with a full width at half maximum of $\approx 0.16^\circ$ performed at BVO(004) peak in the rocking curve measurement (Figure S4, Supporting Information). The epitaxial relationship (i.e., $[001]_{BVO} \parallel [001]_{YSZ}$) of BVO/YSZ was further characterized by aberration-corrected scanning TEM (STEM) as shown in Figure 1b.

Further structure identification by using XRD reciprocal space mapping (RSM) (Figure 1c) taken around YSZ (002) expresses a doublet of BVO (006) along the abscissa, confirming that there are two stacking types of the BVO film relative to c -axis and thus resulting in a multidomain state. The epitaxial relationship can be determined because the c -axis of BVO parallel to that of YSZ. Two alignments of $[100]_{BVO} \parallel [100]_{YSZ}$ and $[010]_{BVO} \parallel [100]_{YSZ}$ for the in-plane conjunction are possible, designated by A and B, respectively (see Figure 1d). Because the YSZ lattice parameter (5.153 Å) is between those of BVO ($a = 5.204$ Å and $b = 5.101$ Å), either in-plane conjunctions are naturally stable. The further identification of the in-plane orientation relationship between the film and substrate is obtained from RSM in Figure 1e. Due to the shear angle along monoclinic $[100]_{BVO}$, a twofold split at least in the BVO (400) is expected. A more complicated domain pattern along the YSZ (400) diffraction in the (HK0) scattering zones is presented, where eight satellites could be distinguished along YSZ (400) and around BVO (200). Based on the RSM results, the corresponding real space lattice is illustrated in Figure 1f, where dash squares represent YSZ reference cubic structure with upward $[001]_{YSZ}$. First, four A domains and four B domains are determined by the reciprocal lattice constant along $[100]_{YSZ}$. Second, due to the combinations of two shear angles (i.e., $\gamma = 90.4^\circ$ and 89.6°) and two deviation angles (φ and 2φ , $\varphi = 0.4^\circ$) from $[100]_{YSZ}$, there are four kinds of alignments for either A or B domains. (The detailed orientation relationship of twin domain features and the method to determine deviation angle φ are described in Figure S5, Supporting Information.) Thus, based on the results of XRD-RSM, the epitaxial relationship is determined, while we speculated the existence of critical material inhomogeneity at the domain wall of ferroelastic multidomain state.

The spatially resolved correlation between domain pattern and flexoelectricity was studied through piezoresponse force microscopy (PFM). The surface height is shown in **Figure 2a**. In-plane PFM phase signal in Figure 2b reveals clear periodic contrast concentrating at domain walls, and it could be concluded that there are four directions of orthogonal domains summarized in the inset of Figure 2b. Moreover, the continuity of phase signal in each bundle domain^[20,21] suggests that the signal results from the piezoresponse, rather than the crosstalk of topography because the discontinuity on surface shows no phase signal. The line section of height and in-plane phase signal at one bundle domain are extracted to Figure 2c, in which alternative A and B domains exist. Here we would like to emphasize the piezoresponse appeared at domain wall area with alternative phase value, and the visualization of in-plane piezoresponse vector fields is built by angle-resolved

Y. Ivry
Solid State Institute Technion
Israel Institute of Technology
Haifa 3200003, Israel

Y.-C. Chen
Department of Physics
National Cheng Kung University
Tainan, Taiwan

Y.-H. Chu
Department of Materials Science and Engineering
National Tsing Hua University
Hsinchu 30013, Taiwan

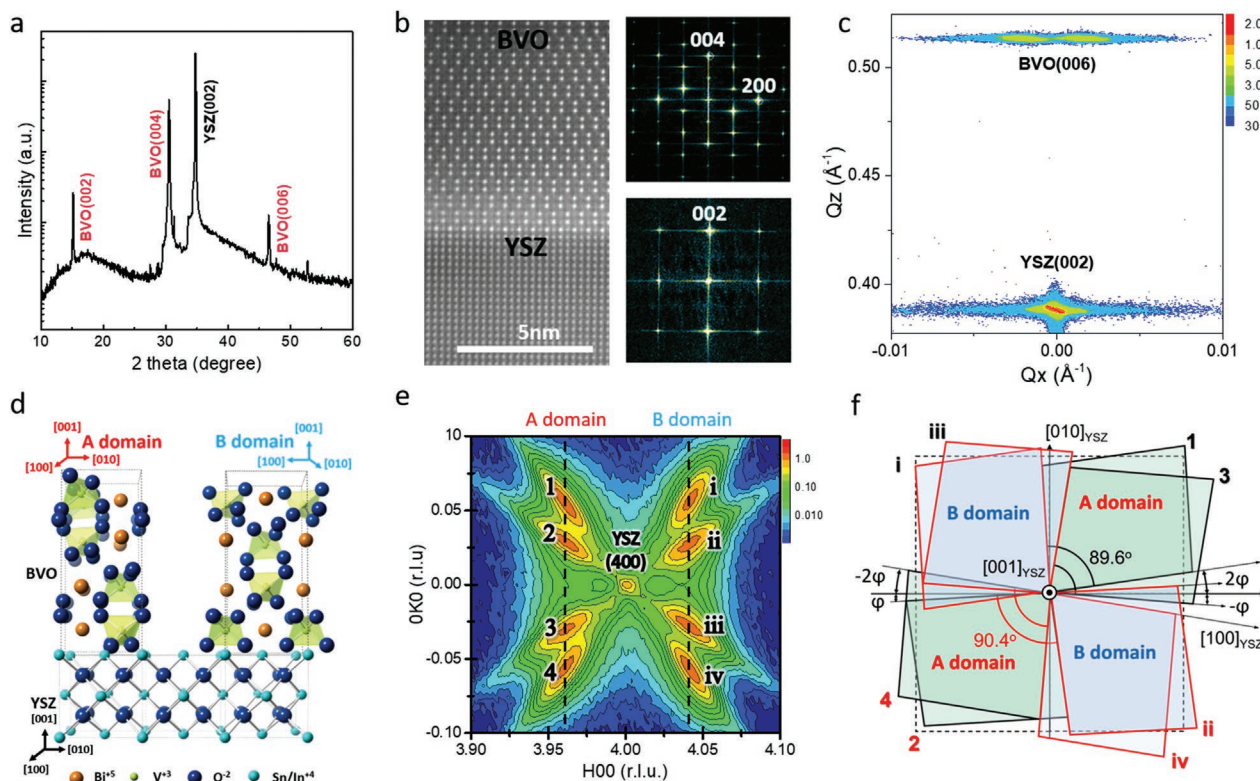


Figure 1. Characterization of BVO films. a) Out-of-plane XRD theta-2theta scan of the heterostructure. b) Cross-HAADF-STEM image at the interface. The corresponding FFT patterns of BVO and YSZ are clearly indexed. The zone axis is $[010]_{\text{YSZ}}$. c) RSM of BVO (006) with YSZ (002) reference for a 100-nm-thick film in the (HOL) scattering zones. d) Schematic of the epitaxial relationships of A and B domains with the YSZ substrate. An A domain represents epitaxial relationship of $[100]_{\text{BVO}} \parallel [100]_{\text{YSZ}}$, while a B domain corresponds to $[010]_{\text{BVO}} \parallel [100]_{\text{YSZ}}$. e) RSM of BVO (400) with YSZ (400) reference for a 100-nm-thick film in the (HKO) scattering zones. f) Schematic of the orientation relationship between A, B domains of BVO, and the YSZ substrate. The detailed description is in Figure S5 (Supporting Information).

(AR) PFM in Figure S6 (Supporting Information). The configuration of lattice transition at domain wall is illustrated in Figure S2 (Supporting Information). It represents that each bundle domain contains 180° head-to-head piezoresponse vector at neighboring domain walls. Unlike ferroelectrics, the direction of domain in Figure 2b and flexo-polarity are unrelated to specific crystal axis due to the form of incommensurate domain wall.^[22] In addition, the amplitude of out-of-plane PFM signal (Figure S7c, Supporting Information) is negligible compared to the in-plane one (Figure S7e, Supporting Information). The amplitude of PFM signal is operated at the resonance frequency of in-contact cantilever, so that this giant difference is remarkable. The PFM data show that in BVO, the strain gradient across a domain-wall area (calculated in Text S1, Supporting Information) lowers the local symmetry,^[23] and results in the piezoresponse mainly along in-plane direction. These results are consistent with the structure inhomogeneity in the wall position between A and B domains due to the difference between the a and b parameters of BVO. Furthermore, the internal electric field and the corresponding surface potential were detected by Kelvin probe force microscopy (KPFM).^[24] However, since the KPFM is operated in lift mode, the spatial resolution is less than the PFM analysis, and it has difficulties in resolving the surface potential at the desired location: the relatively narrow domain walls. Therefore, the

noise level of surface potential is larger than the signal in Figure S7g (Supporting Information).

The direct observation of periodic ferroelastic A/B twin structures is clearly revealed in plane-view STEM image taken along the zone axis of $[001]_{\text{YSZ}}$ in Figure 2d. Figure 2e represents high-angle annular dark-field scanning transmission electron microscopy (HAADF)-STEM image and schematic lattice structures of A and B domains. The local domain type is determined by comparing the fast Fourier transform (FFT) of both A and B domains in Figure S8 (Supporting Information), and the diffraction pattern acquired in an A domain region matches that received from a B domain region with a 90.37° ($1.07^\circ + 89.3^\circ$) counterclockwise difference, indicating the twofold symmetry. The multiple domains of BVO create inhomogeneous distribution of spontaneous strain especially along in-plane direction at domain walls.

To further validate the flexoelectric effect and understand the role of domain walls with atomic resolution, the visualization of strain field by the geometric phase analysis (GPA) was conducted. Figure 2f shows the plane-view STEM image containing A and B domains, and $(\bar{2}20)$ as well as (220) facets in the diffraction pattern (in Figure 2g) were selected as g_1 and g_2 for analysis. Maps of the local shear strain field ($\epsilon_{xy} \approx 2\%$ in Figure 2h) and lattice rotation ($\omega_{xy} \approx 1.2^\circ$ in Figure 2i) are more pronounced compared with the normal strain fields (ϵ_{xx} and ϵ_{yy})

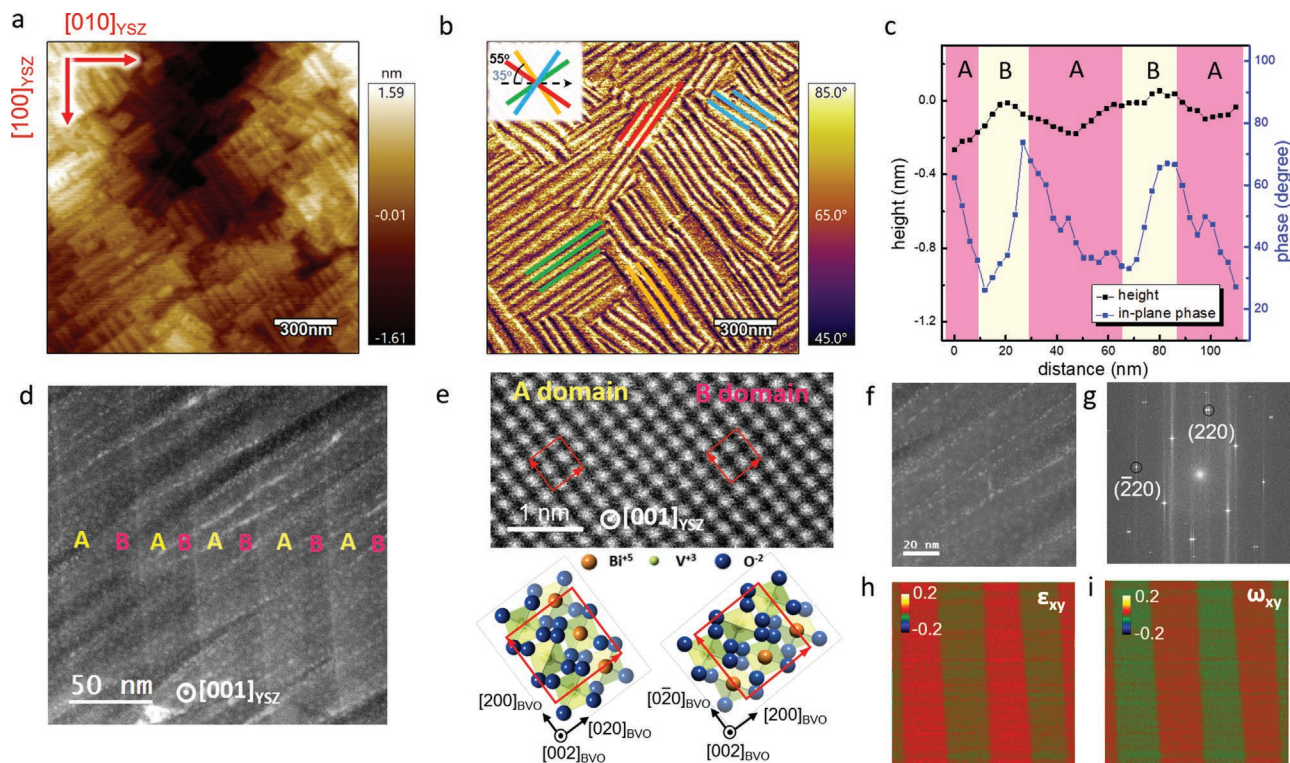


Figure 2. In-plane PFM and strain field characteristics. a) The topography of BVO/YSZ film. b) The according in-plane PFM phase signal recorded simultaneously. c) Line section extracted from (a) and (b). d) Plane view HAADF-STEM image at the surface. Diagonal lines are the curtain effect from the FIB preparation procedure. e) High-resolution plane-view HAADF-STEM images taken along the $[001]_{\text{YSZ}}$, and a schematic diagram of unit cells of A domain and B domain. The red boxes represent monoclinic unit cells of these domains. The way to identify A and B domains is demonstrated in Figure S8 (Supporting Information). f) STEM image of plane view lattice along $[001]_{\text{YSZ}}$ zone axis. g) FFT of the area. (220) and $(\bar{2}20)$ were selected as g_1 and g_2 for mathematical analysis. h) ϵ_{xy} and i) ω_{xy} were deduced by GPA.

as shown in Figure S9 (Supporting Information). Although the normal strain field is negligible, the evaluated shear strain gradient in Figure 2i ($\approx 5 \times 10^6 \text{ m}^{-1}$) across the domain walls leads to the piezoresponse by flexoelectricity, which is also predicted by molecular dynamics simulations in the previous study.^[25] The direct observation of strain gradients ($\approx 5 \times 10^6 \text{ m}^{-1}$ in Figure S9h, Supporting Information) is comparable with the calculated value ($\approx 4.23 \times 10^6 \text{ m}^{-1}$ in Text S2, Supporting Information), and such a strain gradient is an universal effect instead of occasional phenomenon since the in-plane strain gradient distributes throughout the film (cross-sectional STEM and GPA in Figure S10, Supporting Information). Furthermore, the neighboring domain walls represent opposite shear strain gradients, which is responsible for 180° head-to-head piezoresponse at neighboring domain walls in Figure S2 (Supporting Information). Combined with the relationship of domain width and film thickness (Figure S11, Supporting Information), the strain distribution is strongly affected by the material inhomogeneity rather than the substrate clamping effect (Text S2, Supporting Information). Based on the results of PFM, strain field analysis and direct observation of strain gradient, the origin of piezoresponse is believed to arise from the reduction of symmetry at domain wall area from flexoelectricity.

Given that the lattice misfit and the reduction of symmetry at domain walls induce the substantial strain gradients and result in a piezo-response triggered by the flexoelectric effect,

the direct connection between ferroelastic nature and piezoresponse could be built by in situ modulation of temperature, especially focusing on the phase transformation. When the temperature is above the Curie temperature of BVO,^[26] the ferroelastic monoclinic phase would transform into the paraelastic tetragonal one. Due to the increase of symmetry in crystal structure (i.e., from monoclinic I_2/b to tetragonal I_4/a), we expect the spontaneous strain gradient across domain wall would disappear as well. In Figure 3a, when the temperature was increased to 135°C , the splitting satellites assemble in contrast to room temperature RSM taken along the YSZ (400) reflection (Figure 1c), implying not only the expansion of b -axis, but also the contraction of a -axis in BVO. When the temperature increased to 225°C (Figure 3b), the splitting diffraction peaks are barely visible, while the deviation angle is near zero. After the phase transformation at 325°C (Figure 3c), the tetragonal diffraction spot of BVO (400) overlaps with that of YSZ (400), indicating a coherent heteroepitaxy ($a_{\text{BVO, tetragonal}} = a_{\text{YSZ, cubic}}$). Figure 3d shows the change of lattice parameter with temperature. The lattice misfit between A and B domains could be calculated ($\text{misfit} = \frac{a_m - b_m}{a_m} = 2\%$) based on the lattice parameters of monoclinic phase of BVO. The lattice misfit also reduces to 0 after the phase transition at 325°C . Typically, elastic domains are a form of strain releasing mechanism that arises during a phase transition that is accompanied by symmetry lowering.^[27]

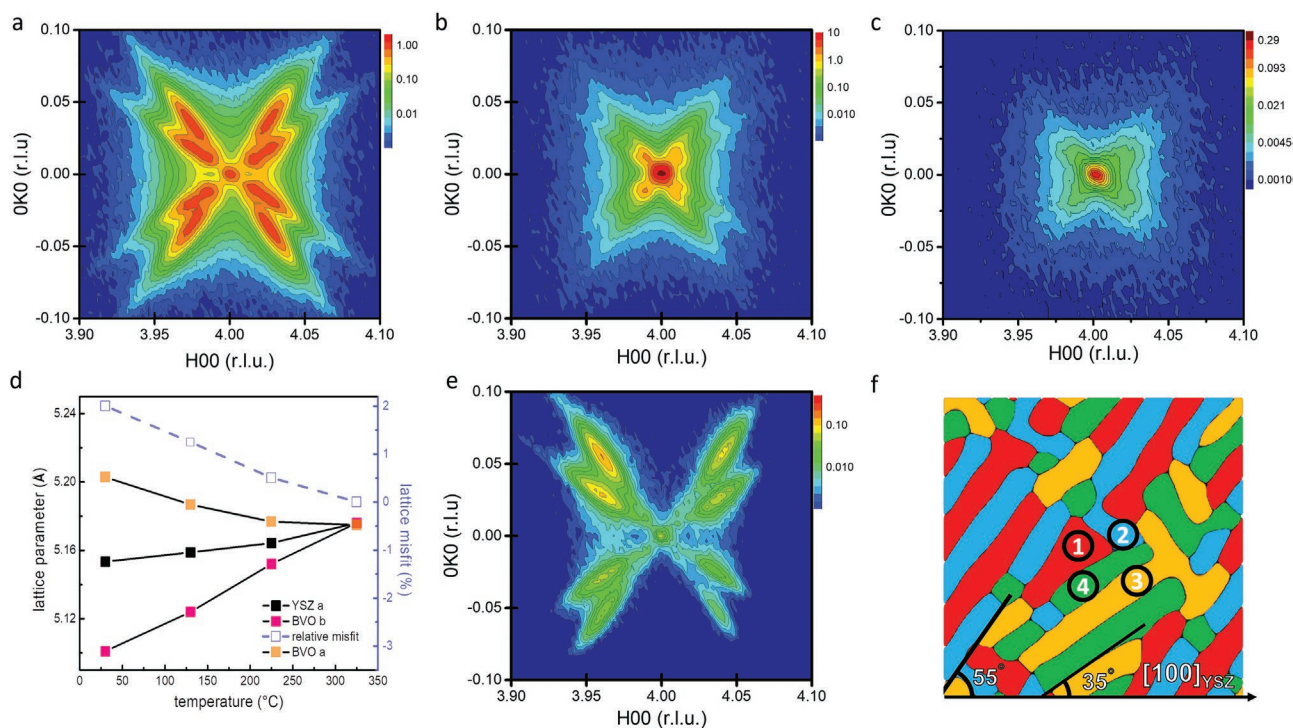


Figure 3. Temperature dependent characteristics of BVO/YSZ thin film. In-plane RSM of BVO (400) with YSZ (400) reference a) At 130 °C. b) At 225 °C. c) At 325 °C. d) Variation of lattice parameters with temperature. e) In-plane RSM of BVO (400) with YSZ (400) reference after thermal process and back to room temperature. f) Phase field simulation of orthogonal twin domain configuration.

Here, the crystal structure changes while the film is compatible to the substrate. Thus, strain is accumulated at the tethered film and is partially released by forming poly-domains that comprise sets of alternating A and B domains with different crystallographic orientation. Therefore, when it cools down to room temperature, the satellites appear as those initially observed (Figure 3e), featuring the reversibility of the phase transition. The asymmetric feature of satellites in Figure 3e might result from the misalignment after the thermal process. The phase transition temperature is determined to be 270 °C by temperature dependent XRD theta-2theta scan (Figure S12, Supporting Information). Since the space group is transformed from I_2/b to high temperature $I4_1/a$, the selection rule eliminates the reflection condition (i.e., $l = 3n$). Thus, the extinction of (006) diffraction peak marks the phase transition while the displacement of (004) diffraction peak reflects the thermal expansion effect.

In order to understand the evolution of ferroelastic twin domains in BVO/YSZ heterostructure, the phase-field simulation was employed. As presented in Figure 3f, there are two conclusions: (i) variant 1 (red color) and variant 2 (blue color) form a striped-like twin-domain configuration, while variant 3 (yellow color) and variant 4 (green color) form the other; (ii) every variant reveals two perpendicular orientations, arising from mechanically compatible ferroelastic domain walls.^[28] The results of the phase-field simulations are consistent with the experimental observation (Figure 2b). The formation of ferroelastic twin domains is induced by the spontaneous strain during the phase transition.^[29,30] Also, the orientation angles of

twin domain walls for variant 1 and 2, and for variants 3 and 4 are about 35° and 55° from phase-field simulations. The width of twin domain for 20-nm-thickness BVO film is ≈ 22 nm, in agreement with that of the experimental fitting results (≈ 23 nm) in Figure S11 (Supporting Information).

Furthermore, high temperature in situ TEM and PFM^[31] were carried out to gain insights into domain transformation. Plane-view TEM images in Figure S13 (Supporting Information) display A/B domains with four directions of bundle domains in agreement with Figure 2b. With the increase of temperature, a strain relaxation process is mediated by the domain wall motion at 250 °C, implying the beginning of phase transition from the monoclinic phase to the tetragonal one. The vanishment of domain pattern reflects the transition temperature of 250–275 °C, which is in agreement with the macroscopic phenomenon in the XRD results. In addition, the twin domain structure reconstructs after cooling down to room temperature, showing the reversibility of phase transition. **Figure 4** displays in-plane PFM signal with temperature dependence. The inserted white curves mark the edge of bundle domain and in-plane domain distribution at room temperature. The domain structure was then recorded in the temperature range from 25 to 275 °C (Figure S14, Supporting Information). When the temperature increased to 200 °C (Figure 4b), the marked bundle domain was penetrated by a surrounding domain with 90° domain wall, while other domains remained. In addition, this phenomenon became more pronounced with a rise of temperature to 230 °C (Figure 4c). Compared with Figure 4a, the marked bundle domain was interrupted by surrounding

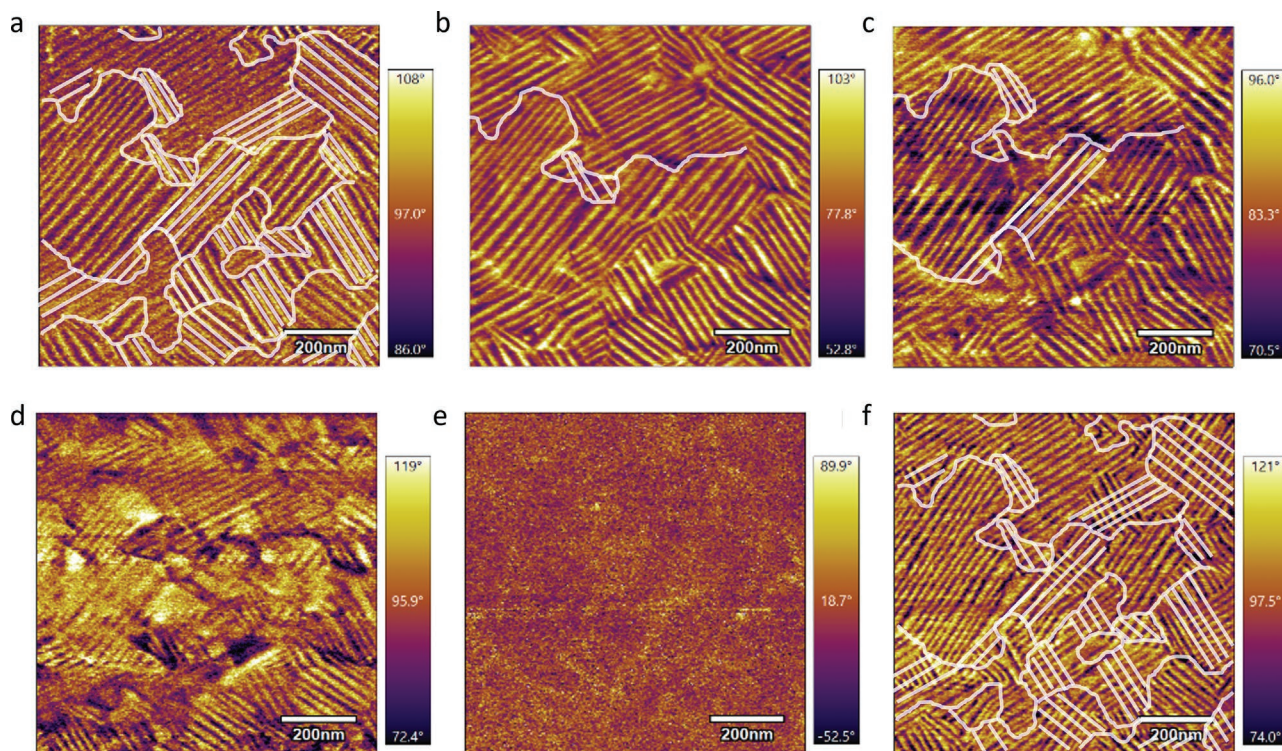


Figure 4. Temperature dependent characteristics of BVO/YSZ thin film. The high temperature analysis of PFM: The in-plane phase signal of BVO a) at room temperature, b) at 200 °C, c) at 230 °C, d) at 260 °C, e) at 275 °C, f) after the heating process and cooling down to room temperature. For high temperature PFM analysis, the single crystal diamond conducting probe was used due to its superior durability and stable resolution.

domains, creating new domain walls. At 260 °C (Figure 4d), some of the twin domains became barely visible, which implies the beginning of the phase transform instead of the thermal artifact since the resonance signal of in-contact scanning tip remained at high temperature (Figure S15, Supporting Information). In addition, above the phase transition point of 275 °C, the in-plane phase signal indeed vanishes (in Figure 4e), which means BVO undergoes the phase transformation to the paraelastic phase. This phenomenon could be explained by the reducing of the lattice misfit in Figure 3d, because the in-plane flexoelectric effect results from the in-plane lattice misfit in ferroelastics. Moreover, in Figure 4f, after cooling down to room temperature and reaching the stable state after few days, the new-formed stripes of domain as well as the PFM signal emerge again, featuring the generation of piezoresponse and its dependence on the phase transition. Based on the above results, it is concluded that the formation of piezoresponse at ferroelastic twin domain walls are induced by the spontaneous strain gradient during the tetragonal to monoclinic phase transition based on flexoelectricity.

Since BVO is well known for its potential for solar energy conversion, strategies focus on expanding lifetime of photo-carriers. For example, band structure engineering technique based on heterojunction promotes carrier-separation ability, such as BaTiO₃/BVO ferroelectric-semiconductor hybrid^[32] or FeOOH/BVO heterojunction.^[33] Beside, tuning oxidation/reduction of V_{OV}⁵⁺/V_{OV}⁴⁺ states in BVO^[34] or modulation of oxygen vacancy by hybrid structure^[35] provides insights to modify carrier

trapping/extracting procedure. In addition, ferroelectric-semiconductor hybrid (Iodide-doped BiVO₄/BaTiO₃)^[36] could also be applied to piezophototronic field, which is an coupling effect between photoexcitation and piezopotential. Aside from recent studies, this work systematically investigates polar domain walls unforeseen from its symmetry, revealing that the flexoelectricity originated from domain walls could possibly endow a flexopotential for charge transport.

3. Conclusion

Over the past decades, the emergence of polar domain walls in ferroelastics has been widely studied since the forbidden characteristic by symmetry is surprising revealed, launching new research direction of utilizing material inhomogeneity. Here, we systematically analyzed the flexoelectricity in incommensurate domain walls. The XRD and TEM results confirm the ferroelastic twin domain features of BVO film. Substantial in-plane PFM signal further verifies the 180° head-to-head domain wall lying on in-plane direction. Based on the GPA results, the electric field inside domain walls is attributed from the shear strain gradient between adjacent twin domains. The ferroelastic-paraelastic phase transition was probed by temperature dependent RSM, plane-view STEM and in-plane PFM analysis. This work investigates the flexoelectric effect is induced at domain walls of ferroelastic BVO system, and we further speculate that the spontaneous in-plane electric field would therefore

promote separation of electron-hole pairs to improve the photocatalytic performances.

4. Experimental Section

Sample Preparation: BVO epitaxial film was deposited on YSZ substrate via pulsed laser deposition.^[37] YSZ substrates were pre-annealed at 1300 °C for 8 h. The atomic step surface of substrate could be obtained and is shown in Figure S1 (Supporting Information). The KrF excimer laser ($\lambda = 248$ nm, COMPex 102, Coherent) was operated at laser fluence of 1 J cm⁻² using commercial BVO target. The deposition temperature was kept at 550 °C and an oxygen pressure was maintained at 60 mTorr. After the deposition, the cooling rate was 25 °C min⁻¹. The thickness of thin film was modulated by the number of pulses and the growth rate was determined to be ≈ 0.05 Å per pulse (see Figure S11, Supporting Information).

X-Ray Diffraction: XRD investigation was performed at Bruker D2 Discover XRD System with Cu K α x-ray ($\lambda = 1.5406$ Å) to obtain the θ -2 θ scan along normal direction at room temperature. The temperature dependent RSMs were conducted by synchronism based high-resolution 8 circle diffractometer at beamline 17B at the National Synchrotron Radiation Research Center in Hsinchu, Taiwan. The incident beam with energy of 10 keV and size 0.3×0.7 mm² was adopted. These RSMs were recorded in reciprocal lattice unit that is normalized by referencing (001)-oriented YSZ substrate.

Electron Microscopy Characterization and Analysis: The cross-sectional TEM specimen was thinned to less than 30 μ m first by mechanical polishing. The subsequent argon ion-beam milling was carried out using PIPS (Model 691, Gatan Inc.) with the accelerating voltage of 3.5 kV until a hole was made. Low voltage milling was performed with accelerating voltage of 0.3 kV to remove the surface amorphous layer. Part of HAADF-STEM images were recorded at an aberration corrected FEI (Titan Cubed Themis G2) operated at 300 kV. The convergence semi-angle for imaging was 30 mrad, the collection semi-angles snap was 39–200 mrad. GPA was based on the STEM image using Gatan Microscopy Suite software. The TEM specimens used for plane-view were prepared by focused ion beam equipment (GAIA3 GMH SEM-FIB, Tescan). HAADF and ABF images were collected by a double aberration corrected STEM (JEM ARM300CF, JEOL) operated at 300 kV. All high-resolution ABF images were raw data without any post filtering. The in situ evolution of the twin domains was recorded with a TEM (JEM-2100F, JEOL), operating at temperatures ranging from room temperature to 300 °C.

Piezoresponse Force Microscopy: PFM was carried out on a commercial SPM system (Asylum Research MPF-3D) using commercial Platinum coating tips (mikromasch HQ:NSC36/PT, cantilever C, resonance frequency = 65 kHz) for room temperature and diamond tips (Adama AD-2.8-AS, resonance frequency = 65 kHz) for high temperature analysis, because single crystal diamond conducting probe display superior durability and stable resolution. Figure 2b and Figure S7 (Supporting Information) were collected at the in-plane contact resonance frequency (about 680 kHz) at DART mode with AC tip bias of 1.5 V. Figure 4, Figure S8 and Figure S15 (Supporting

Information) were performed by vector PFM with out-of-plane contact resonance ≈ 300 kHz and lateral resonance ≈ 680 kHz.

Phase-Field Modeling: In the phase-field simulations, four order parameters of η_1 , η_2 , η_3 , and η_4 , for four variants of M-phase were used. The total energy of the BVO film consists of bulk energy, gradient energy, and elastic energy is expressed as,

$$F_{\text{total}}(\eta_1, \eta_2, \eta_3, \eta_4) = \int_V (f_{\text{bulk}}(\eta_1, \eta_2, \eta_3, \eta_4) + f_{\text{gradient}}(\eta_1, \eta_2, \eta_3, \eta_4) + f_{\text{elastic}}(\eta_1, \eta_2, \eta_3, \eta_4)) dV \quad (1)$$

where f_{bulk} consists of polynomial of η_i^2 , η_i^4 and $\eta_i^2 \eta_j^2$ ($i, j = 1, 2, 3, 4$, but $i \neq j$), f_{gradient} consists of the gradient of η_i ($i = 1, 2, 3, 4$), and f_{elastic} can be expressed by $f_{\text{elastic}} = \frac{1}{2} c_{ijkl} e_{ij} e_{kl}$ (i.e., e_{ij} is elastic strain). The simulated 3D grids of $256 \Delta x \times 256 \Delta y \times 36 \Delta z$ with $\Delta x = \Delta y = \Delta z = 1$ nm were used to describe a 3D constrained system consisting of the bottom substrate layer (= 12 Δz), BVO thin film (= 20 Δz) and the top air layer (= 4 Δz). Thin film boundary conditions were utilized. A spectral iteration method for heterogeneous system was used to obtain the elastic solution.^[38,39]

Supporting Information

Supporting Information is available from the Wiley Online Library or from the author.

Acknowledgements

This work was supported by Ministry of Science and Technology, Taiwan (Grant No. MOST 109-2124-M-009-009-, MOST 109-2124-M-009-001-MY3, MOST 109-2634-F-009-028, MOST 106-2112-M-001-036-MY3, MOST 109-2112-M-001-043-MY3) and the Center for Emergent Functional Matter Science of National Chiao Tung University from The Featured Areas Research Center Program within the framework of the Higher Education Sprout Project by the Ministry of Education (MOE) in Taiwan. R.-C.P. acknowledges the support from Natural Science Foundation of China under Grant No. 51902247 and Natural Science Foundation of Shanxi Province under Grant No. 2020JQ-059. P.G. acknowledges the support from the Key R&D Program of Guangdong Province (2018B030327001, 2018B010109009). Y.I. thanks the Zuckerman STEM Leadership Program as well as Ministry of Science and Technology, Israel, for financial support. Z.Q., J.H., and S.L. acknowledge the support from Westlake Education Foundation and the computational resource from Westlake University HPC Center.

Conflict of Interest

The authors declare no conflict of interest.

Data Availability Statement

The data that support the findings of this study are available in the supplementary material of this article.

Keywords

BiVO₄, centro-symmetric systems, domain walls, flexoelectrics, phase transitions

Received: December 5, 2021

Revised: February 5, 2022

Published online: March 24, 2022

- [1] S. Tokunaga, H. Kato, A. Kudo, *Chem. Mater.* **2001**, *13*, 4624.
- [2] D. Zhou, L.-X. Pang, D.-W. Wang, I. M. Reaney, *J. Mater. Chem. C* **2018**, *6*, 9290.
- [3] X. Yao, X. Zhao, J. Hu, H. Xie, D. Wang, X. Cao, Z. Zhang, Y. Huang, Z. Chen, T. Sritharan, *iScience* **2019**, *19*, 976.
- [4] L. Zhang, D. Chen, X. Jiao, *J. Phys. Chem. B* **2006**, *110*, 2668.
- [5] S. Yun, K. Song, K. Chu, S.-Y. Hwang, G.-Y. Kim, J. Seo, C.-S. Woo, S.-Y. Choi, C.-H. Yang, *Nat. Commun.* **2020**, *11*, 4898.
- [6] G. F. Nataf, M. Guennou, J. M. Gregg, D. Meier, J. Hlinka, E. K. H. Salje, J. Kreisel, *Nat. Rev. Phys.* **2020**, *2*, 634.
- [7] R. K. Vasudevan, Y. Cao, N. Laanait, A. Ievlev, L. Li, J.-C. Yang, Y.-H. Chu, L.-Q. Chen, S. V. Kalinin, P. Maksymovych, *Nat. Commun.* **2017**, *8*, 1318.
- [8] S. Y. Yang, J. Seidel, S. J. Byrnes, P. Shafer, C. H. Yang, M. D. Russell, P. Yu, Y. H. Chu, J. F. Scott, J. W. Ager, L. W. Martin, R. Ramesh, *Nat. Nanotechnol.* **2010**, *5*, 143.
- [9] E. Salje, H. Zhang, *Phase Transitions* **2009**, *82*, 452.
- [10] J. F. Nye, P. P. L. J. F. Nye, *Physical Properties of Crystals: Their Representation by Tensors and Matrices*, Clarendon Press, Oxford **1985**.
- [11] H. Yokota, Y. Uesu, *J. Appl. Phys.* **2021**, *129*, 014101.
- [12] R. Munprom, P. A. Salvador, G. S. Rohrer, *Chem. Mater.* **2014**, *26*, 2774.
- [13] E. Prince, *International Tables for Crystallography, Volume C: Mathematical, Physical and Chemical Tables*, Springer, Netherlands **2004**.
- [14] S. H. Choh, M. S. Jang, *Mater. Res. Express* **2016**, *3*, 045021.
- [15] W. I. F. David, I. G. Wood, *J. Phys. C: Solid State Phys.* **1983**, *16*, 5127.
- [16] C. Hill, M. C. Weber, J. Lehmann, T. Leinen, M. Fiebig, J. Kreisel, M. Guennou, *APL Mater.* **2020**, *8*, 081108.
- [17] Y. K. Kshetri, B. Chaudhary, T. Kamiyama, T.-H. Kim, F. Rosei, S. W. Lee, *Mater. Lett.* **2021**, *291*, 129519.
- [18] A. W. Sleight, H. y. Chen, A. Ferretti, D. E. Cox, *Mater. Res. Bull.* **1979**, *14*, 1571.
- [19] T. H. Yeom, S. H. Choh, K. J. Song, M. S. Jang, *J. Phys.: Condens. Matter* **1994**, *6*, 383.
- [20] J. F. Scott, A. Hershkovitz, Y. Ivry, H. Lu, A. Gruverman, J. M. Gregg, *Appl. Phys. Rev.* **2017**, *4*, 041104.
- [21] Y. Ivry, D. P. Chu, C. Durkan, *Nanotechnology* **2010**, *21*, 065702.
- [22] J. E. Massad, R. C. Smith, *J. Intell. Mater. Syst. Struct.* **2003**, *14*, 455.
- [23] P. Zubko, G. Catalan, A. Buckley, P. R. L. Welche, J. F. Scott, *Phys. Rev. Lett.* **2007**, *99*, 167601.
- [24] L. Yang, S. K. Ravi, D. K. Nandakumar, F. I. Alzakia, W. Lu, Y. Zhang, J. Yang, Q. Zhang, X. Zhang, S. C. Tan, *Adv. Mater.* **2019**, *31*, 1902963.
- [25] E. K. H. Salje, S. Li, M. Stengel, P. Gumbsch, X. Ding, *Phys. Rev. B* **2016**, *94*, 024114.
- [26] W. I. F. David, A. M. Glazer, A. W. Hewat, *Phase Transitions* **1979**, *1*, 155.
- [27] S. P. Alpay, A. L. Roytburd, *J. Appl. Phys.* **1998**, *83*, 4714.
- [28] P. Marton, I. Rychetsky, J. Hlinka, *Phys. Rev. B* **2010**, *81*, 144125.
- [29] Y. Wang, A. G. Khachatryan, *Acta Mater.* **1997**, *45*, 759.
- [30] M. Mamivand, M. Asle Zaeem, H. El Kadiri, L.-Q. Chen, *Acta Mater.* **2013**, *61*, 5223.
- [31] A. Hershkovitz, F. Johann, M. Barzilai, A. Hendler Avidor, Y. Ivry, *Acta Mater.* **2020**, *187*, 186.
- [32] L. Yang, D. K. Nandakumar, L. Miao, L. Suresh, D. Zhang, T. Xiong, J. V. Vaghasiya, K. C. Kwon, S. Ching Tan, *Joule* **2020**, *4*, 176.
- [33] L. Yang, D. K. Nandakumar, L. Suresh, S. Zhang, Y. Zhang, L. Zhang, J. Wang, J. W. Ager, S. C. Tan, *ACS Nano* **2021**, *15*, 19119.
- [34] S. Selim, E. Pastor, M. García-Tecedor, M. R. Morris, L. Francàs, M. Sachs, B. Moss, S. Corby, C. A. Mesa, S. Gimenez, A. Kafizas, A. A. Bakulin, J. R. Durrant, *J. Am. Chem. Soc.* **2019**, *141*, 18791.
- [35] B. Zhang, S. Yu, Y. Dai, X. Huang, L. Chou, G. Lu, G. Dong, Y. Bi, *Nat. Commun.* **2021**, *12*, 6969.
- [36] X. Zhou, B. Shen, J. Zhai, N. Hedin, *Adv. Funct. Mater.* **2021**, *31*, 2009594.
- [37] Y.-L. Huang, H.-J. Liu, C.-H. Ma, P. Yu, Y.-H. Chu, J.-C. Yang, *Chin. J. Phys.* **2019**, *60*, 481.
- [38] S. Y. Hu, L. Q. Chen, *Acta Mater.* **2001**, *49*, 1879.
- [39] L. Q. Chen, J. Shen, *Comput. Phys. Commun.* **1998**, *108*, 147.